Title	Conditions for late gadolinium enhancement MRI in myocardial infarction model rats that better reflect microscopic tissue staining
Author(s)	Ueda, Junpei; Kurata, Hayato; Ota, Miwa et al.
Citation	Scientific Reports. 2024, 14, p. 18308
Version Type	VoR
URL	https://hdl.handle.net/11094/98248
rights	This article is licensed under a Creative Commons Attribution-NonCommercial-NoDerivatives 4.0 International License.
Note	

scientific reports

OPEN

Conditions for late gadolinium enhancement MRI in myocardial infarction model rats that better reflect microscopic tissue staining

Junpei Ueda[1,2], Hayato Kurata[3], Miwa Ota[3], Isamu Yabata[1,4], Koji Itagaki[1,5], Reika Sawaya[1,4], Chiharu Murata[3], Natsuo Banura[1,6], Hiroyuki Nishida[3] & Shigeyoshi Saito[1,6✉]

Late gadolinium enhancement (LGE) is a widely used magnetic resonance imaging method for assessing cardiac disease. However, the relationship between different LGE signal thresholds and microscopic tissue staining images is unclear. In this study, we performed cardiovascular MRI on myocardial infarction (MI) model rats and evaluated the relationship between LGE with different signal thresholding methods and tissue staining images. We prepared 16 rats that underwent MRI 14–18 days following a surgery to create an MI model. We captured cine and LGE images of the cardiac short-axis and longitudinal two- and four-chamber views. The mean ± 2SD, ± 3SD, and ± 5SD of the pixel values in the non-infarcted area were defined as the LGE area. We compared areas of Sirius red staining, determined by the color tone, with their respective LGE areas at end-diastole and end-systole. We observed that the LGE area calculated as the mean ± 2SD of the non-infarcted area at end-diastole demonstrated a significant positive correlation with the area of Sirius red staining (Pearson's correlation coefficient in both: 0.81 [$p < 0.01$]). Therefore, the LGE area calculated as the mean ± 2SD of the non-infarcted area at end-diastole best reflected the MI area in tissue staining.

Myocardial infarction (MI) is a major cause of mortality worldwide[1]. Some of the widely used treatments for MI include percutaneous coronary intervention, coronary artery bypass grafting, and thrombolytic therapy[2–6]. Assessment of myocardial viability using noninvasive imaging techniques is relevant for the efficacy of these therapies[7,8] such techniques need to be able to accurately represent the area of MI to maximize treatment efficacy.

Cardiovascular magnetic resonance (CMR) imaging is a non-invasive technique for imaging MI. It can provide a variety of information such as cardiac function[9], relaxation time measurement[10,11], strain analysis[12,13], and flow velocity measurement[14,15]. As in the clinical setting, CMR has also been used in preclinical studies on the animal heart[16–21]. One CMR technique that highlights the area of myocardial injury is late gadolinium enhancement (LGE). LGE uses gadolinium contrast agent. Although gadolinium contrast agent is contraindicated in subjects with impaired renal function, gadolinium contrast agent adds information and is essential in MRI studies. Gadolinium contrast agent is distributed in the extracellular fluid and shortens both T1 and T2 of the surrounding protons. The areas where gadolinium contrast agent accumulates produce high signals, contributing to differential diagnosis of tumors, etc.[22–24]. LGE is a method that utilizes the delayed arrival and washout of gadolinium contrast agent in fibrotic regions of the myocardium[25]. Furthermore, in acute myocardial infarction, rupture of the cell membrane of the damaged myocardial cell allows the gadolinium contrast agent to be present in the intracellular space, which is not possible in normal myocardial cells[26]. The damaged cardiomyocytes are

[1]Division of Health Sciences, Department of Medical Physics and Engineering, Osaka University Graduate School of Medicine, Suita, Osaka 560-0871, Japan. [2]Department of Radiological Sciences, Faculty of Health Sciences, Morinomiya University of Medical Sciences, Osaka 559-8611, Japan. [3]ROHTO Pharmaceutical Co., Ltd, Kizugawa, Kyoto 619-0216, Japan. [4]Division of Radiology, Department of Medical Technology, Osaka University Hospital, Osaka 564-8565, Japan. [5]Division of Clinical Radiology Service, Kyoto University Hospital, Kyoto 606-8507, Japan. [6]Department of Advanced Medical Technologies, National Cardiovascular and Cerebral Research Center, Suita, Osaka 564-8565, Japan. ✉email: saito@sahs.med.osaka-u.ac.jp

also replaced by a collagen matrix over time. This replacement causes an expansion of the intercellular space and an increase in the area of distribution of the gadolinium contrast agent.

For the above reasons, the LGE technique is capable of delineating fibrotic areas as high-signal areas. Because the pattern of delayed contrast differs depending on the disease, LGE is widely used in diagnostic imaging for cardiac disease[27]. In myocardial infarction, the pattern of LGE is predominantly endocardial, and as the disease progresses, the area of LGE expands to the epicardium. It is also used for assessment of myocardial viability[28]. Viability assessment uses the rate of progression of the LGE area, from endocardial to epicardial, as a predictor of the effect of revascularization.

LGE has been reported to accurately reflect the infarcted area in stained tissues[29–31]. Methods for calculating the area of LGE have included signal thresholding using the standard deviation (SD) and full width at half maximum (FWHM)[32]. These methods do not identify the delayed contrast area visually but can automatically calculate the delayed contrast area based on the area of normal or abnormal myocardium. However, these previous studies have reported comparisons of LGE in ex vivo and microscopic tissue staining image. There have not been many reports on the relationship between LGE signal thresholding methods in in vivo and microscopic tissue staining images.

The purpose of this study was to acquire CMR images of MI model rats and evaluate the relationship between LGE with different signal thresholding methods and tissue staining images.

Material and methods
Animal preparation
We report this animal study in accordance with the ARRIVE guidelines. All the experimental protocols were approved by the Research Ethics Committee of Osaka University, Osaka, Japan (Number: R02-05-0). All experimental procedures involving animals and their care were carried out in accordance with the University Guidelines for Animal Experimentation and the National Institute of Health's Guide for the Care and Use of Laboratory Animals. Experiments were performed on sixteen 8-week-old male Wistar rats, purchased from Japan SLC (Hamamatsu, Japan). All rats were housed in a controlled vivarium environment (24 °C; 12:12 h light–dark cycle) and fed a standard pellet diet with water ad libitum. The MI models were established through surgical ligation of the left anterior descending coronary artery using a 7-0 polypropylene suture. For the procedure, the rats underwent tracheal intubation and were anesthetized with 3% isoflurane for induction and 1–2% isoflurane for maintenance of anesthesia. MRI was performed on the model rats 14–18 days followed the surgery.

Magnetic resonance imaging
MR images of the animal hearts were acquired using a horizontal 7T-MRI system (PharmaScan 70/16 US; Bruker Biospin, Ettlingen, Germany) equipped with a transmit/receive volume radiofrequency coil with a diameter of 60 mm. The rats were positioned with their mouths in a stereotaxic frame to prevent movement in the prone position during scanning and were maintained at a body temperature of 36.5 °C by water flow regulation. They were continuously respiratory monitored using a physiological monitoring system (SA Instruments Inc., Stony Brook, NY, USA). All MRI rat experiments were performed under general anesthesia with 1.0–2.0% isoflurane in an air–oxygen mixture (Abbott Laboratories, Abbott Park, IL, USA) administered through a mask covering the nose and mouth. The respiratory rate of the rats was controlled by increasing or decreasing the anesthesia dose so as to keep the rate at about 70 breaths per minute.

Short- and long-axis two-chamber and long-axis four-chamber images were obtained using fast low-angle shots (FLASH) with a self-gated magnetic resonance cine imaging system. For short-axis images, the following parameters were used: repetition time (TR)/echo time (TE) = 40.0/2.2 ms, flip angle = 25°, movie frames = 14 frames per cardiac cycle, field of view (FOV) = 42.0 × 42.0 mm, in-plane resolution per pixel = 219 μm, matrix = 192 × 192, slice thickness = 2 mm, number of excitations (NEX) = 1, oversampling = 250, acquisition time = 21 min 20 s, and five concomitant slices covering the whole heart from the apex to the base. For the long-axis two- and four-chamber views, the parameters were TR / TE = 6.1/3.0 ms, flip angle = 10°, movie frames = 14 frames/cardiac cycle, FOV = 42.0 × 42.0 mm, in-plane resolution per pixel = 219 μm, matrix = 192 × 192, slice thickness = 2 mm, NEX = 1, oversampling = 250, acquisition time = 3 min 37 s, and one slice through the center of the heart.

LGE images were also obtained using FLASH with a self-gated magnetic resonance cine imaging system. First, 0.3 ml of gadolinium contrast agent (ProHance injections; Bracco-Eisai Co.,Ltd.) was administered through the tail vein and imaging was performed 5 min after administration. For LGE images, the following parameters were then used: TR/TE = 40.0/2.2 ms, flip angle = 25°, movie frames = 14 frames per cardiac cycle, FOV = 42.0 × 42.0 mm, in-plane resolution per pixel = 219 μm, matrix = 192 × 192, NEX = 1, oversampling = 250, acquisition time = 3 min 37 s, and one slice at the same position as the third slice in the short-axis cine image. The total scan time per animal was approximately 40 min.

Sirius red staining for assessment of cardiac fibrosis
For the evaluation of fibrotic alterations in the heart tissues, all hearts were removed immediately after euthanasia. Euthanasia was performed by 5% isoflurane in an air–oxygen mixture administered through a mask covering the nose and mouth. The removed hearts were fixed in 10% neutral buffered formalin. The heart tissues were dehydrated, embedded in paraffin, sectioned at a 4-μm thickness, and stained using Sirius red for histopathological analysis at the short-axis slice of the mid-left ventricle. The extent of cardiac fibrosis was assessed in Sirius red-stained tissue specimens under a microscope (Axio Scan.Z1; Carl Zeiss, Oberkochen, Germany).

MRI data analysis

The cardiac MR images were analyzed using Cvi42 software (Circle Cardiovascular Imaging, Calgary, AB, Canada, https://www.circlecvi.com/cardiac-mr). To identify the left myocardial area, borders of the epicardium and endocardium were manually outlined on the short-axis cine images at both the end-diastolic and end-systolic phases. The left ventricular end-diastolic volume (LVEDV), left ventricular end-systolic volume (LVESV), left ventricular stroke volume (LVSV), and left ventricular ejection fraction (LVEF) were calculated from the short-axis cine images. In addition, myocardial wall thickness at end-diastole and end-systole in each American Heart Association (AHA) segment were calculated from short- and long-axis two-chamber cine images. All values were calculated automatically using Cvi42.

A region of interest (ROI) was manually placed in the ventricular septum as a reference for the non-infarcted area, which was determined to be the ventricular septum based on visual microscopical evaluation of the tissue staining and LGE images. The mean $\pm 2SD, \pm 3SD$, and $\pm 5SD$ of the pixel values in the non-infarcted area were defined as the LGE area. The measurement of LGE was expressed as the percentage of LGE area in the entire left ventricular myocardium. The percentage of LGE area in the left ventricular myocardium was calculated at both end-diastole and end-systole. Again, all values were calculated automatically using Cvi42.

Analysis of tissue staining images

Microscopic tissue staining images were analyzed using ImageJ software (National Institutes of Health, Bethesda, MD, USA). Using color deconvolution, one of ImageJ's functions, the original stained images were classified into three types according to their color tone: stained color images (fibrotic myocardial areas), unstained color images (nonfibrotic myocardial areas), and background area color images. The ROI extracting the color tones was manually placed and made as small as possible, and the images were enlarged as much as possible. The original and stained color images were automatically binarized using the software. ROIs were then manually placed on the left ventricular endocardium, epicardium, and the inner and outer leaflets of the left ventricular myocardium in each binarized image. The ROIs in the endocardium and epicardium were identical between the binarized original image and the binarized stained color image. The ratio of the number of pixels in the stained areas of the left ventricular myocardium to the total number of pixels in the left ventricular myocardium was determined by subtracting the number of pixels between the ROIs in the endocardium and epicardium and the number of pixels in the left ventricular myocardium from the binarized original image, and the number of pixels in the stained area of the left ventricular myocardium from the binarized stained color image. This ratio was used to determine the percentage of fibrotic areas of the left ventricular myocardium.

Statistical analysis

All statistical analyses were performed using Prism, version 9 (GraphPad Software, San Diego, CA, USA). The association between any two variables was analyzed by calculating the Pearson's correlation coefficient and using a Bland–Altman plot. Statistical significance was set at $p < 0.05$.

Results

Animals' characteristics and cardiac function

The rats' average body weight was 328.5 ± 51.7 g (Table 1). Figure 1a–f shows representative cardiac cine MR images. In the short-axis view, end-diastolic and end-systolic images showed thinning of the infarcted myocardium from the anterior to the lateral wall (Fig. 1a, d, red arrows). In the four-chamber view, end-diastolic and end-systolic images showed thinning of the infarcted myocardium in the lateral wall on the apical side (Fig. 1b, e, red arrows). Similarly, in the two-chamber view, the systolic images showed thinning of the infarcted myocardium in the anterior wall on the apical side (Fig. 1f, red arrows). In the two-chamber view, the diastolic images did not show thinning of the infarcted myocardium; however, enlargement of the cardiac cavity was observed as in the other figures (Fig. 1c). According to the visual evaluation of cine MRI, the infarction was located anterior to the lateral wall of the apex, which is consistent with the findings described above. Upon measuring cardiac parameters, LVEDV was 0.66 ± 0.11 ml, LVESV was 0.49 ± 0.12 ml, LVSV was 0.18 ± 0.02 ml, and LVEF was $27.6 \pm 7.2\%$ (Table 1). These results showed a decrease in LVEF. In addition, a tendency toward myocardial wall thinning was observed in regions 6, 12, and 16 of the AHA segment (Table 2). Thus, myocardial wall thinning in the anterolateral region of the left ventricular myocardium was also indicated by numerical evaluation.

Late gadolinium enhancement

Figure 2a–f shows representative LGE images. Areas that were not seen before contrast injection were detected on delayed contrast images (Fig. 2a, e). Delayed contrast was observed (Fig. 2b-d, f–h) in the area coinciding with the

Body mass (g)	328.5 ± 51.7
EDV (ml)	0.66 ± 0.11
ESV (ml)	0.49 ± 0.13
SV (ml)	0.18 ± 0.02
EF (%)	27.6 ± 7.2

Table 1. Rat body weight and cardiac function.

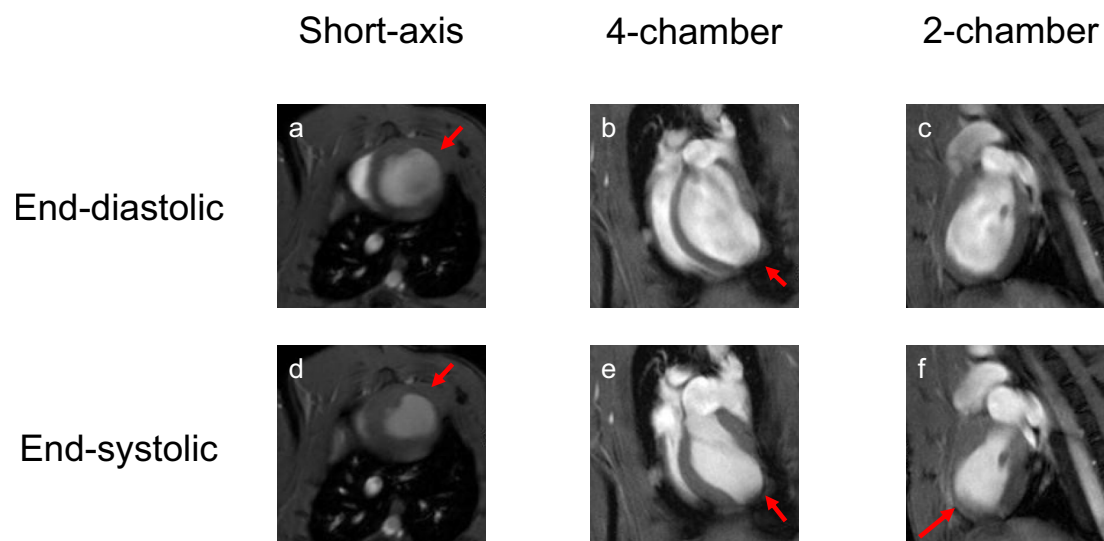|	Short-axis	4-chamber	2-chamber

Figure 1. Representative cardiac cine magnetic resonance images. Short-axis view (**a**, **d**), four-chamber view (**b**, **e**), two-chamber view (**c**, **f**). Images were taken in end-diastolic (**a**, **b**, **c**) and end-systolic (**d**, **e**, **f**) phases of the rat heart. Red arrows: infarcted area.

AHA segment	Thickness of the myocardium (mm)	
	End-diastole	End-systole
1	0.84 ± 0.21	1.33 ± 0.42
2	0.74 ± 0.11	1.32 ± 0.31
3	0.68 ± 0.15	1.50 ± 0.43
4	0.95 ± 0.23	1.80 ± 0.47
5	0.93 ± 0.25	1.18 ± 0.44
6	0.68 ± 0.27	0.88 ± 0.44
7	0.82 ± 0.17	1.10 ± 0.40
8	0.74 ± 0.12	1.43 ± 0.24
9	0.76 ± 0.14	1.64 ± 0.24
10	0.99 ± 0.11	1.49 ± 0.31
11	0.81 ± 0.21	0.93 ± 0.34
12	0.64 ± 0.24	0.74 ± 0.32
13	0.84 ± 0.19	1.01 ± 0.33
14	0.91 ± 0.14	1.59 ± 0.25
15	0.84 ± 0.17	0.93 ± 0.36
16	0.68 ± 0.23	0.65 ± 0.23

Table 2. Thickness of rat left ventricular myocardium at end-diastole and end-systole in each AHA segment region.

area of myocardial thinning identified on cine MRI (Fig. 1). In addition, a tendency to have large areas of delayed contrast was observed at end-systole compared to end-diastole. For the areas calculated as the mean ± 5SD, very few were discriminated as delayed contrast areas (Fig. 2d, h). At end-diastole, the delayed contrast areas calculated as the mean ± 2SD and ± 3SD were 19.7 ± 7.2% and 8.6 ± 5.7%, respectively. At end-systole, the delayed contrast areas calculated as the mean ± 2SD, ± 3SD, and ± 5SD were 23.0 ± 6.6%, 15.1 ± 7.6%, and 3.8 ± 3.2%, respectively.

Sirius red staining of myocardium tissue
Sirius red staining was observed mainly on the lateral wall of the left ventricle (Fig. 3a). The stained areas generally coincided with the delayed contrast areas. The images were segmented into color tones (Fig. 3b–d), and binarized images of the stained areas were created (Fig. 3f). The staining area was calculated from the binarized stained image (Fig. 3f) and the original image (Fig. 3e), and was found to be 18.5 ± 5.2%.
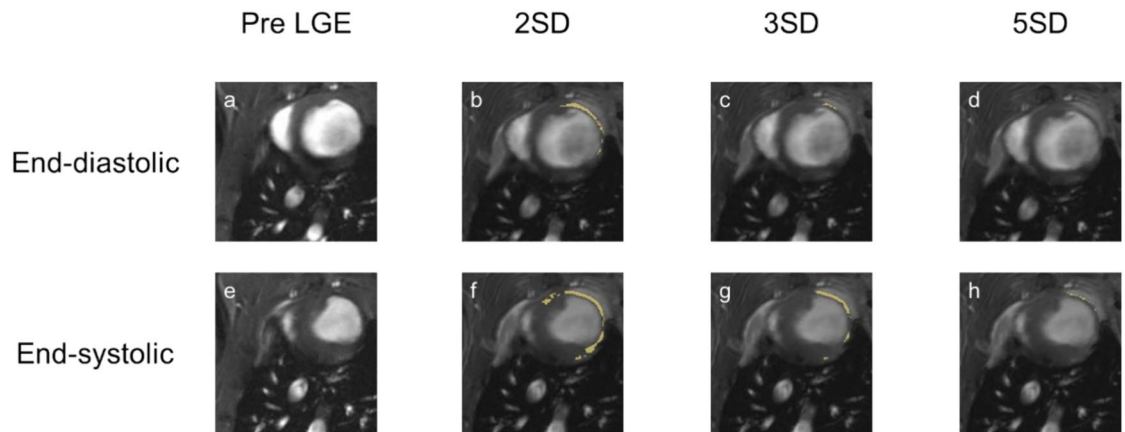
Figure 2. Representative late gadolinium enhancement images. Images before gadolinium contrast administration (**a**, **e**), images of LGE area calculated as mean + 2SD of the non-infected myocardial area (**b**, **f**), images of LGE area calculated as mean + 3SD of the non-infarcted myocardial area (**c**, **g**), images of LGE area calculated as mean + 5SD of the non-infarcted myocardial area (**d**, **g**). Images were taken in end-diastolic (**a**–**d**) and end-systolic (**e**–**h**) phases of the rat heart. Yellow zones: area calculated as LGE.
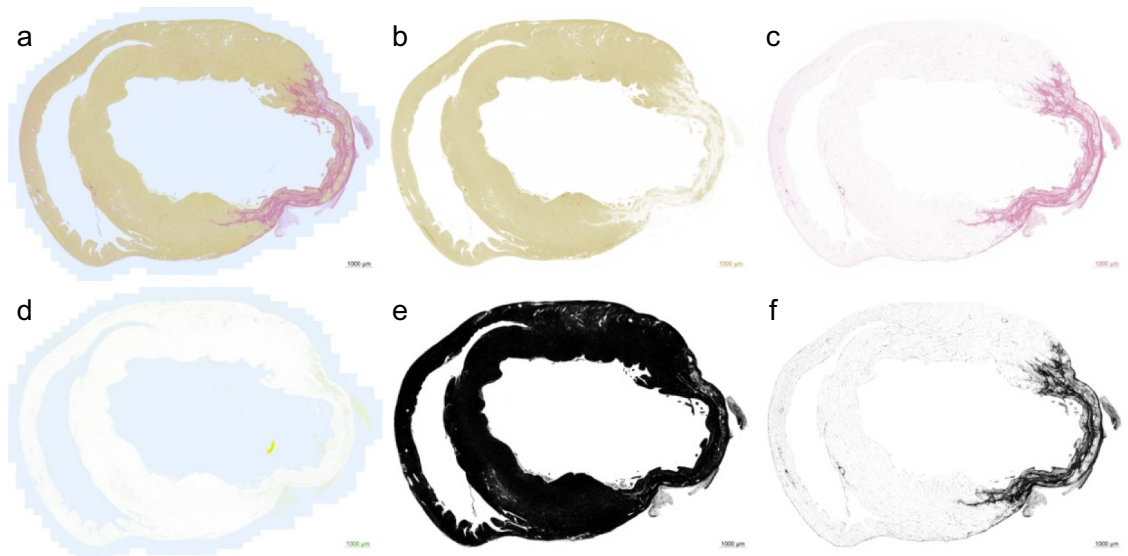
Figure 3. Representative Sirius red stained microscopic images. Original image (**a**). Images of non-stained area (**b**), stained area (**c**), and background area (**d**) were created by dividing the original image by the color tone. Binarized image from original image (**e**), binarized image from the image of stained area (f). This stained image is acquired from the same rat as the LGE image in Fig. 2.

Correlation between LGE images and tissue staining images

From the Bland–Altman plot, the bias between the stained area and LGE area at end-diastole were − 1.2, 9.9, and 17.1 for each delayed contrast area calculated as the mean ± 2SD, ± 3SD, and ± 5SD of the non-infarcted myocardial area, respectively (Fig. 4a–c). Regarding the bias between the stained and LGE areas at end-systole, it was found to be − 4.5, 3.4, and 14.7 for each delayed contrast areas calculated as the mean ± 2SD, ± 3SD, and ± 5SD of the non-infected myocardial area, respectively (Fig. 4d–f). The 95% limits of agreement between the stained and LGE areas calculated as the mean ± 2SD, ± 3SD, and ± 5SD of the non-infected myocardial area were 17.4, 25.3 and 34.1 at end-diastole (Fig. 4a–c) and 25.4, 29.3, and 29.4 at end-systole (Fig. 4d–f), respectively. Pearson's correlation coefficients of the staining with the LGE areas calculated as the mean ± 2SD, ± 3SD, and ± 5SD of the non-infected myocardial area were 0.81 ($p < 0.01$), 0.34, and 0.21 at end-diastole (Fig. 5a–c) and 0.45, 0.41, and 0.17 at end-systole (Fig. 5d–f), respectively.

Discussion

In this study, cardiac cine and LGE images were acquired 14–18 days after the MI surgery, to evaluate cardiac function and degree of myocardial injury. Although CMR images of control rats were not obtained in this study, the LVEF in the rat MI model was decreased here compared to that of previous studies that evaluated cardiac function in normal SD rats[33,34]. On cardiac cine MRI, thinning of the myocardial wall was observed from the
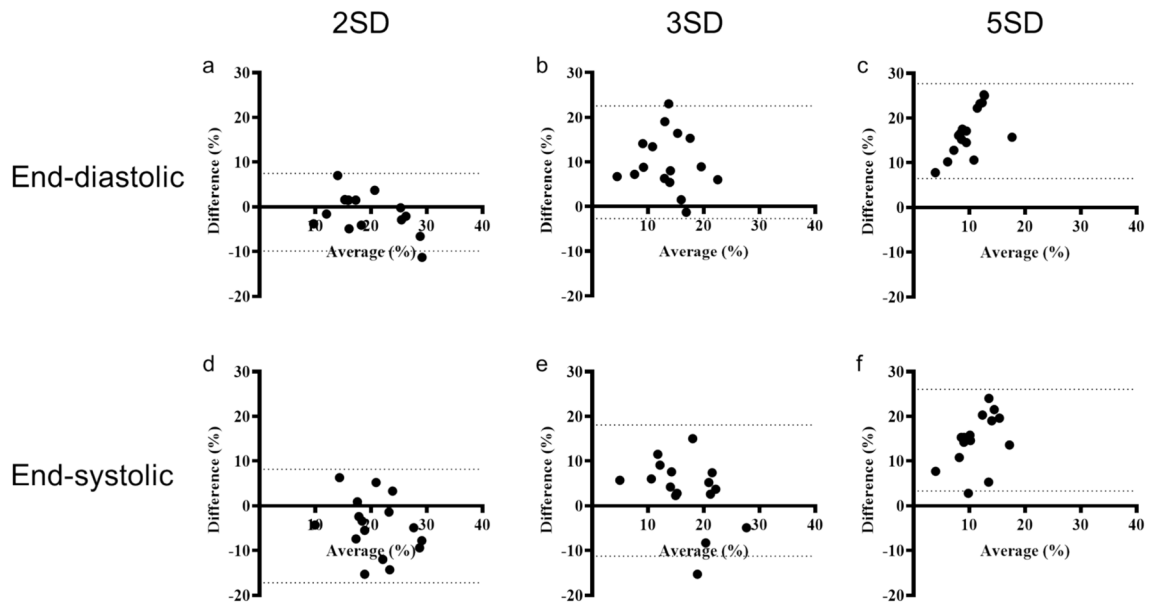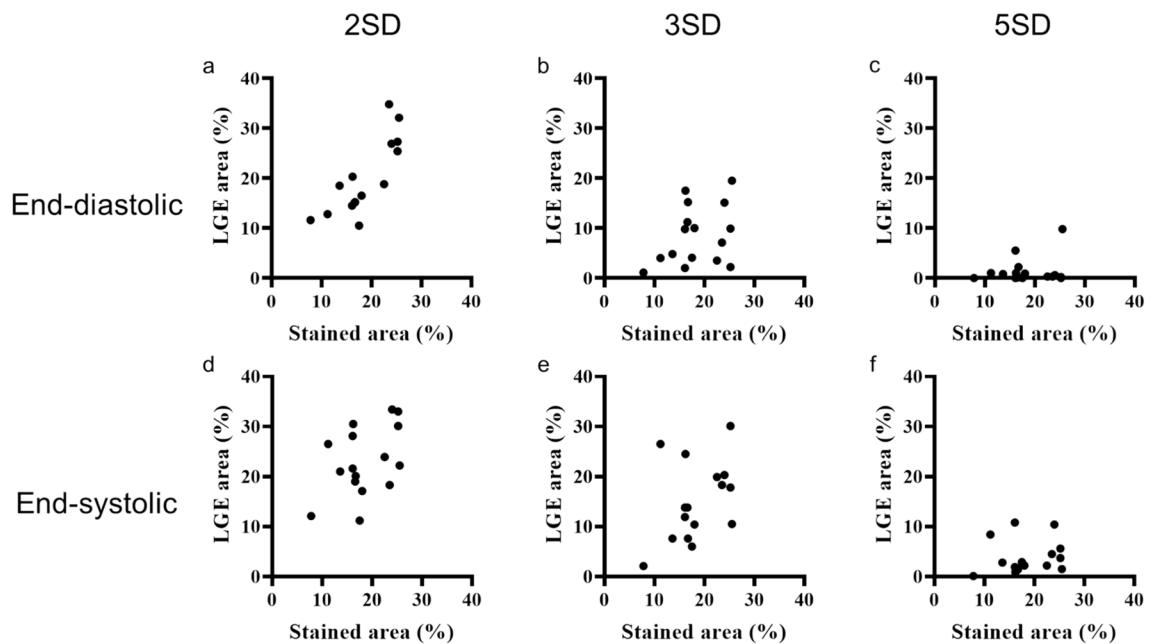
Figure 4. Results of the Bland–Altman plot between Sirius red stained areas and late gadolinium enhancement areas. LGE area calculated as mean + 2SD of the non-infarcted myocardial area (**a, d**), LGE area calculated as mean + 3SD of the non-infarcted myocardial area (**b, e**), and LGE area calculated as mean + 5SD of the non-infarcted myocardia area (**c, f**). Data was collected during end-diastolic (**a–c**) and end-systolic (**d–f**) phases of the rat heart. Dashed line indicates 95% limits of agreement.

Figure 5. Graphs showing the relationship between Sirius red stained areas and late gadolinium enhancement areas. LGE area calculated as mean + 2SD of the non-infarcted myocardia area (**a, d**), LGE area calculated as mean + 3SD of the non-infarcted myocardia area (**b, e**), and LGE area calculated as mean + 5SD of the non-infarcted myocardia area (**c, f**). Data was collected during end-diastolic (**a–c**) and end-systolic (**d–f**) phases of the rat heart.

anterior to the lateral wall of the left ventricle; this area and the LGE areas calculated as the mean ± 2SD, and ± 3SD of the non-infarcted myocardial area were almost matched in visual evaluation. Sirius red staining was also observed from the anterior to lateral wall of the left ventricle. Therefore, the MI model rats in this study had MI from the anterior to the lateral left ventricular wall, and the associated changes in cardiac function and myocardial injury could be detected by MRI. Additionally, the results of the Bland–Altman plots and correlation coefficients showed that the LGE areas calculated as the mean ± 2SD of the non-infarcted myocardial area at end-diastole best represented the degree of staining by Sirius red.

In this study, LGE image acquired at end-systole had a larger contrast enhanced area than those acquired at end-diastole. In addition, the LGE area calculated as the mean ± 2SD of the non-infarcted myocardial area at end-systole tended to be larger than the stained area. Therefore, the LGE area calculated as the mean ± 2SD of the non-infarcted area only at end-diastole was significantly correlated with the stained area. It is widely acknowledged that blood flow in the myocardium is greater during diastole than that during systole. In a previous study, myocardial T1 values changed with changes in the cardiac cycle[35,36]. Although myocardial T1 values were not evaluated in this study, it is possible that the LGE area was similarly affected by changes in the myocardial blood flow due to the cardiac cycle. At systole, when blood flow in the myocardium is low, the increase in the LGE area could be due to an increase in the amount of stagnant gadolinium contrast agent in the myocardium. Furthermore, in a previous study, diseases affecting myocardial perfusion were recommended for evaluation at diastole because of the correlation between myocardial and blood T1 values at diastole[37]. Similarly, the evaluation of LGE imaging in MI was proven to be recommended in diastole, as it better reflects the degree of tissue staining.

Previous studies have made comparisons between LGE images and tissue-stained ones[29,30]. Those studies have also reported a correlation between those areas; however, they used ex vivo specimens to obtain LGE images. In addition, those studies did not include the method of displaying the LGE area in their comparisons. Therefore, this study contributed to the application of these findings in clinical practice, as it involved the use of in vivo rat models for obtaining the LGE images, and showed the conditions for obtaining them that better reflect the tissue-stained area, which is useful for MI studies using LGE images.

Myocardial fibrosis results from the replacement of collagen-rich, extracellular matrix with excess functional tissue[38]. This process is essential for tissue repair to maintain myocardial integrity after injury, but can cause dysfunction such as decreased wall motion[38,39]. Sirius red stains the collagen fibers associated with this fibrosis process. On the other hand, LGE is a technique to display fibrotic areas as high signals, by utilizing the delayed arrival and washout of gadolinium contrast agent in fibrotic areas of the myocardium. Therefore, it is possible that there will be a difference between the area of tissue staining by Sirius red and the area of LGE. In this study, we observed a state close to the chronic phase, 14–18 days after the onset of MI. Therefore, there was little difference between the collagen fiber deposition area and the gadolinium contrast agent stagnation area, and there was little difference between the LGE area and the Sirius red tissue staining area. A similar study should be conducted in the future at a time when there may be a difference between the Sirius red tissue staining area and LGE area in the early stages of collagen fiber deposition, such as in the acute phase of MI. Recent research has reported that early collagen fiber deposition can be detected by T2 mapping[40]. It is important to determine the extent to which LGE can detect myocardial fibrosis by combining various techniques.

This study faced some limitations. First, LGE images were acquired by decreasing the signal of the normal myocardium using a flip angle. However, in clinical practice, sequences based on the Look–Locker method are widely used to acquire LGE image[41]. Therefore, the method of acquiring LGE images in this study differs from the method generally used in clinical practice. Accordingly, this study did not evaluate FWHM based on the abnormal myocardium; therefore, its results are not immediately applicable in clinical practice. Second, only a single LGE imaging condition was examined. Changing the flip angle or other conditions may change the size of the area measured as the LGE area. Therefore, the results of this study may vary depending on the imaging conditions. Third, Sirius red stain was used in tissue staining images when comparing them to LGE image; however, since other tissue staining methods (e.g., Masson-Trichrome staining) can be used to indicate the area of myocardial injury, a comparison between LGE images and images obtained using other tissue staining methods could be investigated in future research. Fourth, the comparison between the LGE and tissue-stained areas was made using the number of pixels in each; therefore, the match between the LGE and the tissue-stained areas was not evaluated in this study. We expect that further research on evaluating the match between these areas will improve the usefulness and reliability of LGE imaging.

Conclusion

In this study, we showed that the LGE area calculated as the mean ± 2SD of the non-infarcted myocardial area better reflects the MI area in microscopic tissue staining images. In addition, we demonstrated that LGE images of MI are most optimally acquired at end-diastole. The application of this knowledge may be useful for the assessment of myocardial viability in clinical practice in the future. Future studies that examine different staining methods may help validate our findings.

Data availability

The datasets generated during and/or analyzed during the current study are available from the corresponding author on reasonable request.

References

1. Tsao, C. W. *et al.* Heart disease and stroke statistics-2023 update: A report from the American Heart Association. *Circulation* **147**, e93–e621. https://doi.org/10.1161/CIR.0000000000001123 (2023).
2. Jensen, L. O. *et al.* Stent thrombosis, myocardial infarction, and death after drug-eluting and bare-metal stent coronary interventions. *J. Am. Coll. Cardiol.* **50**, 463–470. https://doi.org/10.1016/j.jacc.2007.06.002 (2007).
3. Haeck, J. D. *et al.* Randomized comparison of primary percutaneous coronary intervention with combined proximal embolic protection and thrombus aspiration versus primary percutaneous coronary intervention alone in ST-segment elevation myocardial infarction: the PREPARE (PRoximal Embolic Protection in Acute myocardial infarction and Resolution of ST-Elevation) study. *JACC Cardiovasc. Interv.* **2**, 934–943. https://doi.org/10.1016/j.jcin.2009.07.013 (2009).

4. Velazquez, E. J. *et al.* Coronary-artery bypass surgery in patients with ischemic cardiomyopathy. *N. Engl. J. Med.* **374**, 1511–1520. https://doi.org/10.1056/NEJMoa1602001 (2016).

5. Baalaraj, F. S. *et al.* Short and long-term clinical outcomes in octogenarian patients with non-ST-elevation myocardial infarction: A comparative analysis of revascularization strategies versus medical management. *Cureus* **16**, e51430. https://doi.org/10.7759/cureus.51430 (2024).

6. McDonagh, T. A. *et al.* 2021 ESC guidelines for the diagnosis and treatment of acute and chronic heart failure. *Eur. Heart J.* **42**, 3599–3726. https://doi.org/10.1093/eurheartj/ehab368 (2021).

7. Allman, K. C., Shaw, L. J., Hachamovitch, R. & Udelson, J. E. Myocardial viability testing and impact of revascularization on prognosis in patients with coronary artery disease and left ventricular dysfunction: A meta-analysis. *J. Am. Coll. Cardiol.* **39**, 1151–1158. https://doi.org/10.1016/s0735-1097(02)01726-6 (2002).

8. van Loon, R. B., Veen, G., Baur, L. H., Twisk, J. W. & van Rossum, A. C. Long-term follow-up of the viability guided angioplasty after acute myocardial infarction (VIAMI) trial. *Int. J. Cardiol.* **186**, 111–116. https://doi.org/10.1016/j.ijcard.2015.03.152 (2015).

9. Nham, E. *et al.* Association of cardiovascular disease risk factors with left ventricular mass, biventricular function, and the presence of silent myocardial infarction on cardiac MRI in an asymptomatic population. *Int. J. Cardiovasc. Imaging* **32**(Suppl 1), 173–181. https://doi.org/10.1007/s10554-016-0885-1 (2016).

10. Bulluck, H., Dharmakumar, R., Arai, A. E., Berry, C. & Hausenloy, D. J. Cardiovascular magnetic resonance in acute ST-segment-elevation myocardial infarction: Recent advances, controversies, and future directions. *Circulation* **137**, 1949–1964. https://doi.org/10.1161/CIRCULATIONAHA.117.030693 (2018).

11. Langhans, B. *et al.* Reproducibility of area at risk assessment in acute myocardial infarction by T1- and T2-mapping sequences in cardiac magnetic resonance imaging in comparison to Tc99m-sestamibi SPECT. *Int. J. Cardiovasc. Imaging* **30**, 1357–1363. https://doi.org/10.1007/s10554-014-0467-z (2014).

12. Krljanac, G. *et al.* Differences in left ventricular myocardial function and infarct size in female patients with ST elevation myocardial infarction and spontaneous coronary artery dissection. *Front. Cardiovasc. Med.* **10**, 1280605. https://doi.org/10.3389/fcvm.2023.1280605 (2023).

13. Gavara, J. *et al.* Prognostic value of strain by tissue tracking cardiac magnetic resonance after ST-segment elevation myocardial infarction. *JACC Cardiovasc. Imaging* **11**, 1448–1457. https://doi.org/10.1016/j.jcmg.2017.09.017 (2018).

14. Nguyen, L. A. *et al.* Aortic stiffness measured from either 2D/4D Flow and cine MRI or applanation tonometry in coronary artery disease: A case-control study. *J. Clin. Med.* https://doi.org/10.3390/jcm12113643 (2023).

15. Nakamura, S. *et al.* Complementary prognostic value of stress perfusion imaging and global coronary flow reserve derived from cardiovascular magnetic resonance: A long-term cohort study. *J. Cardiovasc. Magn. Reson.* **25**, 20. https://doi.org/10.1186/s12968-023-00930-3 (2023).

16. Hara, A. *et al.* Roles of the mesenchymal stromal/stem cell marker meflin in cardiac tissue repair and the development of diastolic dysfunction. *Circ. Res.* **125**, 414–430. https://doi.org/10.1161/CIRCRESAHA.119.314806 (2019).

17. Onishi, R. *et al.* Application of magnetic resonance strain analysis using feature tracking in a myocardial infarction model. *Tomography* **9**, 871–882. https://doi.org/10.3390/tomography9020071 (2023).

18. Hu, Y. *et al.* Multi-parameter cardiac magnetic resonance imaging detects anthracycline-induced cardiotoxicity in rabbits model. *Heliyon* **9**, e21845. https://doi.org/10.1016/j.heliyon.2023.e21845 (2023).

19. Nahardani, A. *et al.* Pulmonary arteriovenous pressure gradient and time-averaged mean velocity of small pulmonary arteries can serve as sensitive biomarkers in the diagnosis of pulmonary arterial hypertension: a preclinical study by 4D-flow MRI. *Diagnostics (Basel)* https://doi.org/10.3390/diagnostics12010058 (2021).

20. Saito, S. *et al.* Longitudinal observations of progressive cardiac dysfunction in a cardiomyopathic animal model by self-gated cine imaging based on 11.7-T magnetic resonance imaging. *Sci. Rep.* **7**, 9106. https://doi.org/10.1038/s41598-017-09755-4 (2017).

21. Saito, S. & Ueda, J. Preclinical magnetic resonance imaging and spectroscopy in the fields of radiological technology, medical physics, and radiology. *Radiol. Phys. Technol.* **17**, 47–59. https://doi.org/10.1007/s12194-024-00785-y (2024).

22. Kono, M., Adachi, S., Kusumoto, M. & Sakai, E. Clinical utility of Gd-DTPA-enhanced magnetic resonance imaging in lung cancer. *J. Thorac. Imaging* **8**, 18–26 (1993).

23. Chan, A. J. *et al.* Protective effect of aminophylline on renal perfusion changes induced by high-energy shockwaves identified by Gd-DTPA-enhanced first-pass perfusion MRI. *J. Endourol.* **14**, 117–121. https://doi.org/10.1089/end.2000.14.117 (2000).

24. Bendszus, M. *et al.* Gadofluorine M enhancement allows more sensitive detection of inflammatory CNS lesions than T2-w imaging: A quantitative MRI study. *Brain* **131**, 2341–2352. https://doi.org/10.1093/brain/awn156 (2008).

25. Holtackers, R. J. *et al.* Late gadolinium enhancement cardiac magnetic resonance imaging: From basic concepts to emerging methods. *Rofo* **194**, 491–504. https://doi.org/10.1055/a-1718-4355 (2022).

26. Mahrholdt, H., Wagner, A., Judd, R. M. & Sechtem, U. Assessment of myocardial viability by cardiovascular magnetic resonance imaging. *Eur. Heart J.* **23**, 602–619. https://doi.org/10.1053/euhj.2001.3038 (2002).

27. Mahrholdt, H., Wagner, A., Judd, R. M., Sechtem, U. & Kim, R. J. Delayed enhancement cardiovascular magnetic resonance assessment of non-ischaemic cardiomyopathies. *Eur. Heart J.* **26**, 1461–1474. https://doi.org/10.1093/eurheartj/ehi258 (2005).

28. Kim, R. J. *et al.* The use of contrast-enhanced magnetic resonance imaging to identify reversible myocardial dysfunction. *N. Engl. J. Med.* **343**, 1445–1453. https://doi.org/10.1056/NEJM200011163432003 (2000).

29. Kim, R. J. *et al.* Relationship of MRI delayed contrast enhancement to irreversible injury, infarct age, and contractile function. *Circulation* **100**, 1992–2002. https://doi.org/10.1161/01.cir.100.19.1992 (1999).

30. Schelbert, E. B. *et al.* Late gadolinium-enhancement cardiac magnetic resonance identifies postinfarction myocardial fibrosis and the border zone at the near cellular level in ex vivo rat heart. *Circ. Cardiovasc. Imaging* **3**, 743–752. https://doi.org/10.1161/CIRCIMAGING.108.835793 (2010).

31. Wagner, A. *et al.* Contrast-enhanced MRI and routine single photon emission computed tomography (SPECT) perfusion imaging for detection of subendocardial myocardial infarcts: An imaging study. *Lancet* **361**, 374–379. https://doi.org/10.1016/S0140-6736(03)12389-6 (2003).

32. Jada, L. *et al.* Quantification of myocardial scar of different etiology using dark- and bright-blood late gadolinium enhancement cardiovascular magnetic resonance. *Sci. Rep.* **14**, 5395. https://doi.org/10.1038/s41598-024-52058-8 (2024).

33. Zeng, H. T., Zhao, M., Zhang, Z. X., Liu, Z. L. & Zhong, S. M. Atorvastatin improves the cardiac function of rats after acute myocardial infarction through ERK1/2 pathway. *Eur. Rev. Med. Pharmacol. Sci.* **23**, 7120–7127. https://doi.org/10.26355/eurrev_201908_18757 (2019).

34. Fan, Y. Z., Huang, H., Wang, S., Tan, G. J. & Zhang, Q. Z. Effect of lncRNA MALAT1 on rats with myocardial infarction through regulating ERK/MAPK signaling pathway. *Eur. Rev. Med. Pharmacol. Sci.* **23**, 9041–9049. https://doi.org/10.26355/eurrev_201910_19306 (2019).

35. Kawel, N. *et al.* T1 mapping of the myocardium: intra-individual assessment of the effect of field strength, cardiac cycle and variation by myocardial region. *J. Cardiovasc. Magn. Reson.* **14**, 27. https://doi.org/10.1186/1532-429X-14-27 (2012).

36. Wacker, C. M. & Bauer, W. R. Myocardial microcirculation in humans–new approaches using MRI. *Herz* **28**, 74–81. https://doi.org/10.1007/s00059-003-2451-6 (2003).

37. Reiter, U. *et al.* Normal diastolic and systolic myocardial T1 values at 1.5-T MR imaging: Correlations and blood normalization. *Radiology* **271**, 365–372. https://doi.org/10.1148/radiol.13131225 (2014).

38. Kramann, R., DiRocco, D. P. & Humphreys, B. D. Understanding the origin, activation and regulation of matrix-producing myofibroblasts for treatment of fibrotic disease. *J. Pathol.* **231**, 273–289. https://doi.org/10.1002/path.4253 (2013).
39. Shinde, A. V. & Frangogiannis, N. G. Fibroblasts in myocardial infarction: A role in inflammation and repair. *J. Mol. Cell Cardiol.* **70**, 74–82. https://doi.org/10.1016/j.yjmcc.2013.11.015 (2014).
40. Liu, H. *et al.* Early detection of cardiac fibrosis in diabetic mice by targeting myocardiopathy and matrix metalloproteinase 2. *Acta Biomater.* **176**, 367–378. https://doi.org/10.1016/j.actbio.2024.01.017 (2024).
41. Jeuthe, S. *et al.* Myocardial T1 maps reflect histological findings in acute and chronic stages of myocarditis in a rat model. *J. Cardiovasc. Magn. Reson.* **18**, 19. https://doi.org/10.1186/s12968-016-0241-6 (2016).

Acknowledgements

Author contributions

J. U. and S.S. conceived the study; J.U. collected the data with help from H.K., M.O., C.M. H.N. and I.Y, wrote the manuscript and prepared all the figures; J. U., I. Y., and K.I. analyzed the data; I.Y., K.I., R.S., N.B., and S.S. reviewed the manuscript; S.S. obtained the funding.

Competing interests

The authors declare no competing interests.

Additional information

Correspondence and requests for materials should be addressed to S.S.

Reprints and permissions information is available at www.nature.com/reprints.

Publisher's note Springer Nature remains neutral with regard to jurisdictional claims in published maps and institutional affiliations.